

Rebirth of X-ray Emission from the Born-Again Planetary Nebula A 30

M.A. Guerrero¹, N. Ruiz¹, W.-R. Hamann², Y.-H. Chu³, H. Todt², D. Schönberner⁴, L. Oskinova², R.A. Gruendl³, M. Steffen⁴, W.P. Blair⁵, & J.A. Toalá¹
mar@iaa.es

ABSTRACT

The planetary nebula (PN) A 30 is believed to have undergone a very late thermal pulse resulting in the ejection of knots of hydrogen-poor material. Using multi-epoch *HST* images we have detected the angular expansion of these knots and derived an age of 850^{+280}_{-150} yr. To investigate the spectral and spatial properties of the soft X-ray emission detected by *ROSAT*, we have obtained *Chandra* and *XMM-Newton* deep observations of A 30. The X-ray emission from A 30 can be separated into two components: a point-source at the central star and diffuse emission associated with the hydrogen-poor knots and the cloverleaf structure inside the nebular shell. To help us assess the role of the current stellar wind in powering this X-ray emission, we have determined the stellar parameters and wind properties of the central star of A 30 using a non-LTE model fit to its optical and UV spectrum. The spatial distribution and spectral properties of the diffuse X-ray emission is highly suggestive that it is generated by the post-born-again and present fast stellar winds interacting with the hydrogen-poor ejecta of the born-again event. This emission can be attributed to shock-heated plasma, as the hydrogen-poor knots are ablated by the stellar winds, under which circumstances the efficient mass-loading of the present fast stellar wind raises its density and damps its velocity to produce the observed diffuse soft X-rays. Charge transfer reactions between the ions of the stellar winds and material of the born-again ejecta has also been considered as a possible mechanism for the production of diffuse X-ray emission, and upper limits on the expected X-ray production by this mechanism have been derived. The origin of the X-ray emission from the central star of A 30 is puzzling: shocks in the present fast stellar wind and photospheric emission can be ruled out, while the development of a new, compact hot bubble confining the fast stellar wind seems implausible.

Subject headings: planetary nebulae: general – planetary nebulae: individual: A 30 – stars: winds, outflows – X-rays: ISM

¹Instituto de Astrofísica de Andalucía, IAA-CSIC, c/ Glorieta de la Astronomía s/n, 18008 Granada, Spain

²Institute for Physics and Astronomy, Universität Potsdam, 14476 Potsdam, Germany

³Department of Astronomy, University of Illinois, 1002 West Green Street, Urbana, IL 61801, USA

⁴Leibniz-Institut für Astrophysik Potsdam (AIP), An der Sternwarte 16, 14482 Potsdam, Germany

⁵Department of Physics and Astronomy, Johns Hopkins University, Baltimore, MD 21218, USA

1. Introduction

Planetary nebulae (PNe) consist of stellar material ejected by low- and intermediate-mass stars. In the canonical model of PN formation, the so-called interacting stellar winds (ISW) model, the envelope of a star is stripped off through a slow and dense wind and, as the star evolves off the asymptotic giant branch (AGB), it is subsequently swept up by a fast stellar wind (Cerruti-Sola & Perinotto 1985) to form a PN (Kwok, Purton, & Fitzgerald 1978; Balick 1987).

The dynamical structure of a PN can be very complex as the fast stellar wind interacts with a slow AGB wind whose density and velocity structure has been previously modified by the passage of the shock wave associated with a D-type ionization front (Perinotto et al. 2004; Schönberner et al. 2005a,b).

Abell 30 (a.k.a. A 30, PN G208.5+33.2) is a PN with a hydrogen-deficient central star (CSPN) of spectral type [WC]-PG1159 (also termed as “weak emission line stars”). The nebula appears in $H\alpha$ (Figure 1-*left*) as a limb-brightened, presumably spherical shell with a diameter $\sim 2'$, although a close inspection of its kinematics reveals that this shell has a mildly ellipsoidal shape (Meaburn & López 1996). The spherically symmetric limb-brightened morphology, the low surface brightness and the low electron density of this shell (Guerrero & Manchado 1996) are consistent with the expectations for an evolved object in the ISW model of PN formation (e.g., Schönberner et al. 2010). This conjecture is supported by the large kinematical age of 12,500 yr derived from the simple comparison of its angular size, expansion velocity¹ ($38.5 \pm 1.0 \text{ km s}^{-1}$, Meaburn & López 1996) and distance (1.7 kpc, Cahn et al. 1992).

Deep [O III] images of A 30 (Figure 1-*center*) reveal a different picture. The round nebular shell is filled by a delicate system of arc-like features that extend up to $\sim 30''$ from the central star and depict a cloverleaf pattern (Jacoby 1979). More remarkably, a series of knots are detected just a few arcsecs from the central star. These knots are resolved by *HST* Wide Field Planetary Camera 2 (WFPC2) [O III] images (Figure 1-*right*) to be distributed along a disk and two bipolar outflows (Borkowski et al. 1995), a physical structure later confirmed by the spatio-kinematical study carried out by Chu, Chang, & Conway (1997). The knots are found to be extremely faint in H I recombination lines² (Wesson et al. 2003) implying

¹ Even if we accounted for the fact that the real expansion velocity of the shock front is larger by 10%–20% than the observed velocity (Schönberner et al. 2005b), the kinematical age of A 30 would still be large, $\sim 10,500$ yr.

² The [N II] $\lambda\lambda 6548, 6583$ and He II $\lambda 6560$ to $H\alpha$ line ratios for the bipolar knots are ~ 2.1 , ~ 6.3 , and ~ 2.4 , respectively (Wesson et al. 2003). The emission detected at the position of these knots in the $H\alpha$ image (Figure 1-*left*) con-

low content of hydrogen with a He/H abundance ratio of 10.8–11.6 and very high metal abundances of C/H ~ 0.45 , N/H ~ 0.30 and O/H ~ 1.30 (Jacoby & Ford 1983; Guerrero & Manchado 1996; Wesson et al. 2003; Ercolano et al. 2003). These knots and the central star of A 30 are embedded in large amounts of circumstellar dust (Borkowski et al. 1994) with anomalous carbonaceous composition (Greenstein 1981). Apparently, these hydrogen-depleted knots have been ejected only recently by the central star of A 30, in contrast to the old and hydrogen-rich outermost round shell.

The hydrogen-deficient nature of the CSPN of A 30 and the presence of hydrogen-poor ejecta near the star inspired the born-again PN scenario (Iben et al. 1983) (also known as “very late thermal pulse” or VLTP) in which the thermonuclear burning of hydrogen in the remnant stellar envelope builds up the amount of helium until its fusion into carbon and oxygen is ignited (see, e.g., Herwig et al. 1999; Althaus et al. 2005; Lawlor & MacDonald 2006; Miller Bertolami & Althaus 2006; Miller Bertolami et al. 2006, for recent theoretical studies of this phenomenon). Since the remnant envelope is shallow, the increase of pressure from this last helium shell flash leads to the ejection of the newly processed material in the envelope, while the stellar structure remains intact. As the remnant envelope expands, the stellar effective temperature decreases and the star returns to the AGB phase. The stellar evolution that follows this event is fast and will take the star back toward the post-AGB track in the HR diagram (see, e.g., Figures 5 and 8 in Miller Bertolami et al. 2006): the envelope of the star contracts, its effective temperature increases and a new fast stellar wind develops. In a sense, the PN is born-again.

The fast stellar wind will blast the hydrogen-poor material ejected by the star during the born-again event and the subsequent born-again AGB phase. This interaction has been captured by *HST* WFPC2 images of the vicinity of the central star of A 30 (Borkowski et al. 1995). The hydrogen-poor knots of A 30 display a cometary appearance

sists mostly of [N II] and He II emission, rather than $H\alpha$ emission itself, given the 60 Å bandwidth of the $H\alpha$ filter used for these observations.

with either bow-shock structures pointing toward the central star or compact cores with fanning tails pointing away from the central star (Figure 1-*right*) whose expansion velocities increase outward up to $\sim 200 \text{ km s}^{-1}$ (Meaburn & López 1996; Chu, Chang, & Conway 1997). Soft X-ray emission from the mixture of shocked stellar wind and evaporated material can be expected (Borkowski et al. 1995), and has been confirmed by *ROSAT* PSPC serendipitous observations that revealed a source of soft X-ray emission at a plasma temperature $\sim 3 \times 10^5 \text{ K}$ (Chu & Ho 1995). A follow-up *ROSAT* HRI observation showed a central point source and hints of diffuse emission associated with the innermost hydrogen-poor knots, although the detection of the diffuse emission is uncertain due to the low S/N ratio (Chu, Chang, & Conway 1997).

We have obtained *Chandra* and *XMM-Newton* observations of A 30 in order to accurately determine the spatial and spectral properties of its X-ray emission. The results are analyzed in conjunction with the physical properties of its stellar wind determined from refined non-LTE model fits to optical and UV spectra. Multi-epoch *HST* archival images have also been used to search for proper motions of the hydrogen-poor knots in order to assess their angular expansion rate and to investigate their interactions with the fast stellar wind.

In the following, we first investigate in Sect. 2 the stellar wind properties of the CSPN of A 30, given the implications for the X-ray emission, and determine the proper motions of the hydrogen-poor knots in Sect. 3. The X-ray observations and the spatial and spectral properties of the X-ray emission are described in Sect. 4 and the results are discussed in Sect. 5. The conclusions are presented in Sect. 6.

2. Non-LTE Analysis of the CSPN of A 30

Optical and UV spectra of the CSPN of A 30 have been analyzed using calculations performed with the Potsdam Wolf-Rayet (PoWR) model atmosphere code (Hamann & Gräfener 2004, and references therein). This code solves the non-LTE radiative transfer for a spherically expanding atmosphere, accounting for complex model atoms and line blanketing, to derive basic stellar and wind parameters. The calculations applied here

include He, C, N, O, Ne, and the elements of the iron-group (the latter in the superlevel approximation).

The UV spectra of the CSPN of A 30 were observed by the *Far Ultraviolet Spectroscopic Explorer (FUSE)* and *International Ultraviolet Explorer (IUE)* satellites. Data from these observations have been retrieved from MAST, the Mikulski Archive for Space Telescopes at the Space Telescope Science Institute³. The *FUSE* observations of A 30 in the spectral range 920–1180 Å consisted of the data set B0230101 obtained on 2001 April 10 with the LWRS aperture for a total useful exposure time of 4.1 ks (Guerrero & De Marco, in preparation). Similarly, the *IUE* observations of A 30 in the spectral range 1150–3200 Å consisted of the data sets SWP07955LL and LWR06930LL obtained on 1980 February 15 with total exposure times of 1.5 and 3.0 ks, respectively. Complementary high-dispersion optical spectra of the CSPN of A 30 were obtained using the Ultraviolet and Visual Echelle Spectrograph (UVES) on the 8m UT2 of the VLT at Paranal Observatory on 2003 February 19 in the framework of the large project 167.D-0407 (PI: Napiwotzki). The observations consisted of two 300 s exposures that covered the spectral regions 3290–4525 Å, 4605–5610 Å and 5675–6642 Å.

In spite of the limited number of spectral lines useful for analysis provided by the UV and optical spectra of the CSPN of A 30, a reasonable fit (see Fig. 2) is achieved for the set of parameters compiled in Table 1. For the fit we adopted a stellar luminosity of $6,000 L_{\odot}$, noting that the stellar radius, mass-loss rate and distance scale with luminosity according to the relations shown in Table 1. The distance of 1.76 kpc, similar to the statistical distance of 1.69 kpc provided by Cahn et al. (1992), will be used hereafter. The CSPN of A 30 is confirmed to be very hot ($T_{*} = 115 \text{ kK}$), and the emission line spectrum originates from a stellar wind composed predominantly of helium, carbon and oxygen, which is typical for the [WC] spectral type.

Besides small changes in the values of the stellar temperature and helium and carbon abun-

³ The Space Telescope Science Institute (STScI) is operated by the Association of Universities for Research in Astronomy, Inc., under NASA contract NAS5-26555.

dances, the present results do not differ appreciably from those previously reported by Leuenhagen, Koesterke, & Hamann (1993) based on a much earlier version of our model atmosphere code without the inclusion of iron-line blanketing. The major difference between the current and earlier calculations, however, is induced by the inclusion of clumping and mass-loss rate (\dot{M}) effects. In the “microclumping” approximation (e.g., Hamann & Koesterke 1998), the emission line fit yields the product $\dot{M}\sqrt{D}$ where D , the so-called “clumping factor”, is difficult to constrain. The current calculations adopt a value of 10 for D , which has been proven to be an adequate choice for massive WC stars. The only study for the wind of a CSPN (Todt et al. 2008) came to a similar result, although this parameter was poorly constrained. A value of 10 for the clumping factor leads in the present calculations to a mass-loss rate ($\dot{M} = 2 \times 10^{-8} M_{\odot} \text{ yr}^{-1}$) 2.5 times lower than the value derived by Leuenhagen, Koesterke, & Hamann (1993).

According to our calculations, the stellar wind of the CSPN of A 30 has a He:C:N:O element number ratio 100:11:0.7:6.0, i.e., it is carbon rich with a C/O ratio ~ 1.8 . It is interesting to compare these chemical abundances with those of the hydrogen-deficient knots, where the He:C:N:O element number ratio is 100:4.0:2.7:11.6 (Wesson et al. 2003; Ercolano et al. 2003). The low C/O ratio of the hydrogen-poor knots, ~ 0.3 , is at variance with the stellar wind, and is also in contradiction to theoretical models of born-again PNe that predict C/O higher than unity (e.g., Iben et al. 1983; Herwig et al. 1999; Miller Bertolami et al. 2006).

Finally, the spectral fit of the UV and optical spectra of A 30 (Fig. 2) has allowed us to build its spectral energy distribution (SED) shown in Figure 3. The fit of the SED shown in Fig. 3 requires only a small interstellar reddening with $E_{B-V} = 0.18 \pm 0.05$ mag that corresponds to a hydrogen column density $N_{\text{H}} = (6.8 \pm 1.9) \times 10^{20} \text{ cm}^{-2}$ according to the relation $N_{\text{H}}/E_{B-V} = 3.8 \times 10^{21} \text{ cm}^{-2} \text{ mag}^{-1}$ prescribed by Groenewegen & Lamers (1989). We note that the interstellar extinction law of Cardelli et al. (1989) used to deredden the observed spectral data does not reproduce properly the UV absorption at $\sim 2470 \text{ \AA}$ which is attributed to carbonaceous dust (Greenstein 1981),

and thus the value of the hydrogen column density given above is suspect.

3. Proper Motions of the H-poor Knots of A 30

The original *HST* WFPC2 narrow-band [O III] images of A 30 (Fig. 1-*right*) were obtained on 1994 March 6 (epoch 1994.2), but we noticed that the *HST* archive also contained Wide Field Camera 3 (WFC3) images obtained through the F555W filter on 2009 December 31 (epoch 2010.0). It is reasonable to compare these images, taken ~ 15.8 yr apart, because the nebular emission registered by the F555W filter is mostly dominated by the [O III] emission lines. Such comparison indeed unveils the proper motion of the hydrogen-poor knots of A 30, as shown in Figure 4. Following the method used by Reed et al. (1999) to study the angular expansion of NGC 6543, we have magnified the earlier epoch image (the F502N image) by several factors and produced the residual maps shown in Fig. 4. These maps suggest that the hydrogen-poor knots of A 30 have expanded $\sim 2\%$.

A detailed analysis of the location of both bipolar and equatorial knots along different directions in the images of the two epochs has allowed us to refine this result and conclude that the 1994.2 image needs to be magnified by 1.019 ± 0.003 in order to match the 2010.0 image. Such 1.9% expansion in a time lapse of 15.8 yr implies an expansion age of 850_{-150}^{+280} yr that can be interpreted as the time since the born-again episode took place circa AD 1160.

The angular expansion rate can also be used to estimate the averaged expansion velocity of the knots in the equatorial ring. Assuming that the equatorial ring is circular in shape, its major axis lies on the plane of the sky and thus the semi-major axis of $4''.8$ implies a radius of 0.041 pc at a distance of 1.76 kpc. For an age of 850 yr, an averaged expansion velocity of $\sim 50 \text{ km s}^{-1}$ is derived.

Finally, we note the presence of a star $\sim 5''.25$ from the CSPN of A 30 at $\text{PA} \sim 144^\circ$. The possible physical connection of this star with the CSPN of A 30 was used by Ciardullo et al. (1999) to estimate a distance of 2020 pc toward A 30. The comparison between the 1994.2 and 2010.0 epoch images reveals a change of $0''.15$ in the position

of this star relative to the location of the CSPN of A 30. This shift is much larger than the orbital motion expected in the time lapse of 15.8 yr for a companion star with the orbital separation of 10,580 AU estimated by Ciardullo et al. (1999). We therefore conclude that this star and the CSPN of A 30 do not form a binary system, but they are rather optical doubles. Consequently, the distance estimate of 2020 pc is not valid and should not be used.

4. X-ray Observations of A 30

A 30 was observed by *XMM-Newton* on 2009 October 21 (Observation ID 0605360101, PI: W.-R. Hamann) using the European Photon Imaging Camera (EPIC) and the Reflection Grating Spectrometer (RGS) instruments for a total exposure time of 58.2 ks. The EPIC observations were performed in Full Frame Mode with the Thin Filter. The second version of the observation data files (ODFs) generated by the *XMM-Newton* Science Operation Center on 2010 June 18 were processed using the *XMM-Newton* Science Analysis Software (SAS) 10.0.2. Reprocessed EPIC-MOS, EPIC-pn and RGS event lists were created using the SAS tools “emproc”, “eproc” and “rgsproc”, respectively, and the most up-to-date *XMM-Newton* calibration files available on the Current Calibration File (CCF) as of 2010 September 15. The original exposure times were 40.88, 41.08, 37.23, 57.43 and 57.47 ks for EPIC-MOS1, EPIC-MOS2, EPIC-pn, RGS1 and RGS2, respectively, but the last segment of the observations was dramatically affected by periods of high background. After excising these periods from the data, the resulting useful exposure times amount to 31.63 ks for EPIC-MOS1, 31.31 ks for EPIC-MOS2, 24.58 ks for EPIC-pn, 31.81 ks for RGS1 and 31.53 ks for RGS2.

A 30 was subsequently observed by *Chandra* on 2011 January 1 (Observation ID 12385, PI: Y.-H. Chu) using the array for spectroscopy of the Advanced CCD Imaging Spectrometer (ACIS-S) for a total exposure time of 96.09 ks. The nebula was imaged on the back-illuminated CCD S3 using the VFaint mode. No periods of high background affected the data and the resulting useful exposure time amounts to 96.08 ks after excising dead-time periods. The *Chandra* Interactive Analysis

of Observations (CIAO) software package version 4.3 was used to analyze these data.

The *XMM-Newton* EPIC observations detect a relatively bright source at the location of the central star of A 30. An inspection of the images at different energy bands shown in Figure 5 indicates that this source is soft, with emission from the lowest energies detectable by the EPIC cameras up to 0.6 keV, above which little or no emission is seen. Similarly, the *Chandra* observations detected a soft source at the position of the CSPN of A 30. The EPIC-pn, EPIC-MOS and ACIS-S background-subtracted count rates and net number of counts detected in different energy ranges are provided in Table 2.

4.1. Spatial Properties of the X-ray Emission from A 30

In order to study the spatial distribution of the X-ray emission from A 30, we have produced EPIC images of A 30 in different energy bands (Figure 5) by extracting the individual EPIC-pn, EPIC-MOS1 and EPIC-MOS2 images, mosaicing them together, applying the exposure map correction, and smoothing the images. We have also produced a *Chandra* ACIS image in the 200–600 eV energy band. The *Chandra* and *XMM-Newton* X-ray images are compared to optical narrow-band images and previous *ROSAT* X-ray images in Figure 6.

The small-scale spatial distribution of the X-ray emission is revealed by the comparison between the *Chandra* ACIS-S and *HST* WFPC2 [O III] images shown in Figure 6-*left*. Most of the emission detected in the *Chandra* ACIS-S image corresponds to a point source coincident with the central star of A 30, but some additional emission, 8.2 ± 3.5 counts, is found $\sim 4''$ to the southwest of A 30 CSPN. This emission is soft, with a median energy ~ 0.30 keV, and seems spatially coincident with an [O III] bright knot in the equatorial ring of the hydrogen-poor ejecta. Given the extremely low count level of the ACIS-S background in the soft energy band, ~ 0.025 counts arcsec $^{-2}$, the probability that this source were a statistical fluctuation in the background is negligible, $< 10^{-6}$. Furthermore, Figure 6 shows that this source is coincident with one of the brightest patches of diffuse X-ray emission suggested by *ROSAT* HRI images (Chu, Chang, & Conway 1997).

The large-scale spatial distribution of the X-ray emission is illustrated by the comparison between the *XMM-Newton* EPIC and ground-based [O III] images shown in Figures 5 and 6-*right*. The X-ray emission in the *XMM-Newton* EPIC image peaks at the location of the central star, in agreement with the *Chandra* ACIS-S image. The image does not show any obvious diffuse X-ray emission associated with the round outer shell of A 30. Instead, the X-ray peak at the central star is surrounded by a “halo” of diffuse emission whose spatial distribution is consistent with that revealed by *ROSAT* PSPC observations at a poorer spatial resolution (Chu & Ho 1995). There is a tantalizing correlation between the *XMM-Newton* EPIC X-ray contours of this diffuse X-ray emission and the “petals of the cloverleaf” pattern interior to the round outer shell.

To further assess whether this X-ray emission is extended, we have used the SAS 10.0 task “eradial” to extract a radial profile of the X-ray emission from A 30 and fit it to the theoretical *XMM-Newton* EPIC-pn PSF that can be described as a King function with core $5''.5$ and exponent 1.6. However, a direct fit to the radial profile has yielded inconclusive results because A 30 is located at $\sim 70''$ from a chip gap in the EPIC-pn camera, and thus does not allow the extraction of a sufficiently extended radial profile to accurately assess the background level for the PSF fit. The EPIC-MOS images are not useful for this purpose as they lack sufficient statistical significance.

To overcome these difficulties, we have compared a bright, soft point source (Nova LMC1995, Orio et al. 2003) with A 30. A preliminary inspection of the soft images of A 30 and Nova LMC1995 is also inconclusive because Nova LMC1995 also seems to be surrounded by a halo of diffuse emission most likely associated with the PSF of the EPIC-pn. A close comparison of the radial profiles of A 30 and Nova LMC1995 (Figure 7-*left*) built using the SAS task “eradial” finally found evidence suggesting that the radial profile of A 30 departs from that of a point source at distances $>13''$. To reinforce this result, we have also determined the count rate in circular annuli centered on A 30 and Nova LMC1995. The comparison, shown in Figure 7-*right*, confirms that A 30 shows additional emission peaks at distances $>13''$, further strengthening the conclusion that

A 30 displays extended X-ray emission. The limited spatial resolution of the *XMM-Newton* EPIC-pn observations, however, makes it impossible to estimate the extent and distribution of this diffuse emission within $20''$ from the central star of A 30. An attempt to remove the emission from the point source has been made by using a point source model derived from the observation of Nova LMC1995 and scaled to the emission peak of the CSPN of A 30. The residual diffuse emission is basically consistent with the contours shown in Figure 6-*right*.

4.2. Spectral Properties of the X-ray Emission from A 30

To study the spectral properties of the X-ray emission from A 30, we have extracted the EPIC-pn and EPIC-MOS background-subtracted spectra of A 30 shown in Figure 8-*left*. The spectra are extremely soft even when compared to those of diffuse emission from other PNe (e.g., NGC 6543, Chu et al. 2001). The EPIC-pn spectrum, which has the best signal-to-noise ratio, peaks at ~ 0.35 keV with a shoulder or slow decline toward lower energies and a rapid drop in the energy interval from 0.35 keV to 0.5 keV. There is much fainter emission at ~ 0.58 keV, but no further emission is detected above 0.6 keV. A comparison with optically thin plasma emission models of different chemical abundances suggests that the emission at 0.35 keV may correspond to either the C VI lines at 33.7 \AA ($\equiv 0.37$ keV) or the C V lines at 35.0 \AA ($\equiv 0.35$ keV), while the weak feature at 0.58 keV seems consistent with the O VII triplet at 21.8 \AA ($\equiv 0.57$ keV). Similarly, the rapid decline above 0.35 keV seems consistent with plasma emission models for which the contribution from the N VI 0.43 keV and N VII 0.50 keV emission lines is rather small. The RGS spectrum of A 30, despite having a limited signal-to-noise ratio (Figure 8-*right*), has allowed us to identify the emission peak in the EPIC-pn spectrum of A 30 as the Ly α line of C VI at 33.7 \AA ($\equiv 0.37$ keV) and to confirm that there is no significant contribution from nitrogen lines.

Since the analysis of the radial profile of X-ray emission from A 30 reveals extended emission, we have extracted separate spectra for the central source from a circular region of radius $12''$ and for the diffuse emission from an annular region with

a 20'' inner radius and a 35'' outer radius. The background-subtracted EPIC-pn and EPIC-MOS spectra of the central source and diffuse emission are shown in Figure 9 and their count rates and count numbers are listed in Table 2. The comparison of the spectra of the diffuse emission and point source suggests spectral differences, with the diffuse emission spectrum lacking the peak at ~ 0.37 keV associated with the C VI line and having a relatively more important contribution of the O VII triplet at 0.57 keV.

4.3. Spectral Analysis

4.3.1. X-ray Emission Model for A 30

The EPIC and RGS spectra of A 30 imply the presence of emission lines, thus suggesting that the X-ray emission from A 30 can be modeled using an optically thin plasma emission model. The Astrophysical Plasma Emission Code (APEC) v1.3.1 available within XSPEC v12.3.0 (Arnaud 1996) was used for the spectral analysis of the EPIC spectra, adopting the chemical abundances of the stellar wind derived from our non-LTE model listed in Table 1.

Alternatively we may consider charge transfer reactions between heavy ions in the stellar wind and material from the hydrogen-poor knots and dust in the central regions of A 30, as is typically detected in comets in the solar system (e.g., Lisse et al. 1996; Dennerl et al. 1997), as well as in a broad variety of astrophysical objects including the interstellar medium, stellar winds and galaxies (see Dennerl 2010, for a review). The X-ray emission associated with charge transfer reactions in comets can be described by emission lines of the ions involved in these reactions with little or negligible continuum (“bremsstrahlung”) emission. Our model of charge transfer reactions for the X-ray emission from A 30 will consist of the emission lines in the spectral range 0.2–0.7 keV of the most important species in the stellar wind of the CSPN of A 30: C V 0.31 keV, C VI 0.37 keV, N VI 0.43 keV, N VII 0.50 keV, O VII 0.57 keV, and O VIII 0.65 keV.

4.3.2. X-ray Absorption Model for A 30

The X-ray emission from the hot plasma in A 30 is certainly absorbed, but the nature, properties, and amount of the absorbing material

need to be elaborated. The extinction towards the central star of A 30 seems to be relatively high: Cohen et al. (1977), Greenstein (1981), and Jeffery (1995) derived interstellar extinctions of $A_V=0.9\pm 0.1$ mag, $E_{B-V}=0.30$ mag, and $A_V=1.18$ mag, respectively, whereas we have determined it to be $E_{B-V}=0.18\pm 0.05$ mag. As for the extinction towards the central knots, Wesson et al. (2003) derived $c(\text{H}\beta)=0.60$. All these values are in sharp contrast with the low, almost negligible extinction affecting the outer shell of A 30 (Guerrero & Machado 1996), thus suggesting that the origin of the extinction is mostly circumstellar.

The presence of circumstellar dust is indeed revealed by mid-IR and near-IR observations of the innermost regions of A 30 (e.g., Borkowski et al. 1994; Phillips & Ramos-Larios 2007). More recent *Spitzer* archival images (Hart et al. 2011) clearly show the spatial coincidence between the mid-IR emission in the IRAC bands and the disk and bipolar jet features in *HST* [O III] images (Figure 10). The correspondence between the spatial distributions of dust and born-again ejecta and the anomalously high carbon composition of the dust (Greenstein 1981; Jeffery 1995) suggest that this dust is formed by material ejected during the VLTP event. Consequently we will assume that the absorbing material has a chemical composition similar to that of the hydrogen-poor knots, i.e., H:He:C:N:O:Ne = 1:11.2:0.47:0.29:1.33:0.56 by number (Wesson et al. 2003). Although this absorbing material presents noticeable absorptions at the energy of the carbon and oxygen K shells, we must note that at the spectral resolution of the EPIC instruments, the overall shape of the absorption curve of this metal rich material is similar, within a factor 1.5, to that of typical interstellar material.

As for the amount of absorbing material, we have performed a simultaneous spectral fit of the *XMM-Newton* EPIC-pn and EPIC-MOS, and *ROSAT* PSPC spectra of A 30 using an APEC optically thin plasma emission model with stellar wind abundances absorbed by material with the abundances of the hydrogen-poor knots. The fit is not impressively good ($\chi^2/\text{d.o.f.}=199.6/96\sim 2.1$), but it clearly constrains the hydrogen column density at a value $\sim 2\times 10^{15}$ cm $^{-2}$, with a 3- σ upper limit $\leq 1\times 10^{16}$ cm $^{-2}$, for a plasma temperature

of 0.070 ± 0.005 keV (Table 3) and observed flux and intrinsic luminosity in the 0.2-1.5 keV energy range of 1.0×10^{-13} erg cm $^{-2}$ s $^{-1}$ and 4.4×10^{31} erg s $^{-1}$, respectively. Much higher column densities are proscribed by the emission detected in the softest energy channels of the EPIC spectra and very notably of the *ROSAT* PSPC spectrum. We note that the value of the hydrogen column density derived from this fit is significantly smaller than those typical of interstellar material for PNe, in the range 10^{19} – 10^{22} cm $^{-2}$, because the content in helium, carbon and oxygen assumed for the absorbing material is much higher than for the interstellar gas.

Incidentally, we note that the normalization factors of the EPIC and PSPC spectra are similar, within 10%. Given the relative calibration uncertainties, the total X-ray fluxes from A 30 determined by *ROSAT* PSPC on 1993 May and by *XMM-Newton* EPIC on 2009 October are consistent with each other and imply little long-term variability.

4.3.3. Spectral Fits for Plasma Emission

The absorbed APEC optically thin plasma emission model provides a reasonable fit to the EPIC-pn and EPIC-MOS spectra of the diffuse emission for a best-fit value of the temperature $kT = 0.068^{+0.002}_{-0.005}$ keV ($= 0.79 \times 10^6$ K) at a fixed hydrogen column density of 2×10^{15} cm $^{-2}$ (Table 3). The observed flux in the 0.2-1.5 keV energy range is $2.8 \pm 0.9 \times 10^{-14}$ erg cm $^{-2}$ s $^{-1}$, and the intrinsic luminosity is $\sim 1.3 \times 10^{31}$ erg s $^{-1}$.

This same model does not provide a good fit (reduced $\chi^2 \sim 3$) to the EPIC-pn and EPIC-MOS spectra of the central source of A 30 because it cannot reproduce the emission peak at ~ 0.37 keV. The addition of an emission line at this energy improves significantly the fit (Table 3) for a fixed hydrogen column density $N_{\text{H}} = 2 \times 10^{15}$ cm $^{-2}$ and best-fit value of $kT = 0.068 \pm 0.003$ keV ($= 0.79 \times 10^6$ K). For this model we derive an observed flux in the 0.2-1.5 keV energy range of $7.2^{+3.0}_{-1.8} \times 10^{-14}$ erg cm $^{-2}$ s $^{-1}$, and an intrinsic luminosity $\sim 3.1 \times 10^{31}$ erg s $^{-1}$.

The inclusion of an emission line at 0.37 keV is highly indicative of increased emission of the C VI line at 33.7 Å which can be attributed to an enhancement of the carbon abundances or to a

higher temperature plasma component. Neither possibilities seem to work: the enhancement of carbon abundances increases both the emission of the C V and C VI lines without a net improvement of the spectral fit, whereas the inclusion of a higher temperature component produces noticeable emission above 0.45 keV which is not supported by the observed spectrum.

4.3.4. Spectral Fits for Charge Transfer Reactions

In this case, the spectral model consists of the emission lines of C V 0.31 keV, C VI 0.37 keV, N VI 0.43 keV, N VII 0.50 keV, O VII 0.57 keV, and O VIII 0.65 keV at a fixed absorption hydrogen column density of 3×10^{15} cm $^{-2}$. This model also yields good fits for the emission from the CSPN and the diffuse component (Table 4). The intensities of the different emission lines for the best fit models listed in Table 4 indicate that C V 0.31 keV ($\equiv 40.2$ Å) is the prevalent line, with a significant contribution of the C VI 0.37 keV ($\equiv 33.7$ Å) in the central source. Unfortunately, the RGS spectral coverage is limited to the 5–38 Å wavelength range and these observations did not provide confirmation of the prevalence of the C V line. Small contributions of the O VII 0.57 keV ($\equiv 21.8$ Å) line to the diffuse emission and central source are also derived from these fits. On the other hand, the contribution from emission lines of nitrogen is found to be negligible both for the diffuse component and for the CSPN in agreement with its lower abundance in the stellar wind and born-again ejecta.

5. Discussion

The new *Chandra* and *XMM-Newton* observations of A 30 have confirmed the extremely soft X-ray emission previously detected by *ROSAT* PSPC and HRI (Chu & Ho 1995; Chu, Chang, & Conway 1997) and resolved the X-ray emission into a point source and diffuse emission. The comparison between the X-ray and optical images of A 30 allows us to unambiguously associate the X-ray point source with its CSPN. On small angular scales, as probed by *Chandra* and earlier suggested by *ROSAT* HRI images (Chu, Chang, & Conway 1997), the spatial coincidence of the diffuse X-ray emission with the [O III] bright knots (Figure 6-*left*) strongly supports the association of the dif-

fuse X-ray emission with the innermost hydrogen-deficient knots. On larger angular scales, as probed by *XMM-Newton*, the diffuse X-ray emission pervades the central regions of the nebula and fills the cloverleaf structure (Figure 6-*right*). No diffuse X-ray emission is found in the gap between the cloverleaf structure and the edge of the outer round shell.

We next describe in detail the formation and evolution of A 30 in order to assess which processes can be involved in the production of the diffuse and point-source X-ray emission from this nebula.

5.1. Formation and Evolution of A 30

The outer shell of A 30 formed $\sim 12,500$ yr ago from an ordinary AGB wind and was shaped by the stellar radiation field and hydrogen-rich fast wind of the post-AGB star. We see now the relics of this evolution: a large, nearly spherical shell of low density and moderate expansion velocity.

About 850 yr ago, the CSPN of A 30 experienced a VLTP episode which led to the sudden ejection of highly processed hydrogen-poor, carbon-rich material. At that time, the stellar envelope expanded and the star returned to the AGB phase, but shortly afterward the envelope contracted and the star moved to the post-AGB evolutionary track in time-scales as short as 5–20 yr (Iben & MacDonald 1995; Miller Bertolami et al. 2006). We can thus expect that, during the AGB phase after the VLTP episode, a new carbon-rich wind of low speed blew into the nebular cavity. Later, as the star contracted, this carbon-rich wind accelerated up to the present terminal velocity of 4000 km s^{-1} revealed by UV spectra of the CSPN of A 30.

This description of the born-again event and subsequent evolution of the stellar wind of A 30 is limited by our poor understanding of the born-again and post-born-again evolution, based on the very small sample of known born-again PNe, besides A 30: A 58 (a.k.a. V605 Aql, Seitter 1987), A 78 (Jacoby & Ford 1983), and Sakurai’s object (a.k.a. V4334 Sgr, Duerbeck & Benetti 1996). The duration and properties of the wind during the AGB phase after the born-again event are particularly poorly known. In Sakurai’s object, a post-born-again stellar wind with mass-loss rate up to $1.6 \times 10^{-5} M_{\odot} \text{ yr}^{-1}$ (Tyne et al. 2002) and

terminal velocity $\sim 670 \text{ km s}^{-1}$ (Eyres et al. 1999) is detected just a few years after the born-again event. In A 58, the properties of the present stellar wind, with a diminished mass-loss rate of $1 \times 10^{-7} M_{\odot} \text{ yr}^{-1}$ and a terminal velocity $\sim 2500 \text{ km s}^{-1}$ (Clayton et al. 2006), indicate that 82 yr after the VLTP event the star has already returned to the post-AGB evolutive track. It thus seems that, after a born-again event, a post-born-again wind with mass-loss rates 10^{-5} – $10^{-6} M_{\odot} \text{ yr}^{-1}$ and terminal velocity of a few hundred km s^{-1} can be expected for a short phase (few years). This wind is immediately superseded by a fast stellar wind.

The post-born-again and present fast stellar winds will overtake and ablate the hydrogen-poor clumps ejected during the born-again event to produce fanning tails and cavities similar to those predicted by Steffen & López (2004). This interpretation is consistent with the nebular features moving at speeds as high as 200 km s^{-1} that have been associated with the fanning tails of the hydrogen-poor bipolar knots described by Meaburn & López (1996) and Chu, Chang, & Conway (1997). A close inspection of the [O III] echelle spectra presented by Meaburn & López (1996) and those available in the “SPM Kinematic Catalogue of Galactic Planetary Nebulae” (López et al. 2012) reveals faint features along the central line of sight and associated with some cloverleaf features moving at speeds up to 400 km s^{-1} . It is worthwhile to note that similar features, moving at speeds of 250 km s^{-1} , are found in the hydrogen-poor ejecta of A 78 (Meaburn et al. 1998).

These features can be interpreted as signatures of the post-born-again wind in which the hydrogen-poor knots are embedded. We note that the filaments of the cloverleaf structure are not detected in the $\text{H}\alpha$ image, thus suggesting that they consist of hydrogen-poor material. The distance of the outermost cloverleaf filaments to the central star implies a linear size of $1.1 \times 10^{18} \text{ cm}$ that, in conjunction with the age of 850 yr derived in Sect. 3, result in an expansion velocity $\sim 420 \text{ km s}^{-1}$, very similar to the expansion velocity of the post-born-again stellar wind of $\sim 400 \text{ km s}^{-1}$. This suggests that the post-born-again wind may have had a foremost contribution in blowing the cloverleaf structure.

5.2. Origin of the Diffuse X-ray Emission

The ISW model of PN formation predicts the production of a “hot bubble” (Kwok, Purton, & Fitzgerald 1978) filled with X-ray-emitting shocked stellar wind as the result of the interaction of the CSPN fast stellar wind ($v_\infty > 10^3 \text{ km s}^{-1}$) with the previous slow and dense AGB wind ($v_{\text{AGB}} \sim 10 \text{ km s}^{-1}$). X-ray observations of PNe (e.g., Kastner et al. 2000; Chu et al. 2001) have detected the diffuse emission from the shocked stellar wind inside hot bubbles of PNe with X-ray luminosities in the range $7 \times 10^{29} - 2 \times 10^{32} \text{ erg s}^{-1}$ (Ruiz et al., in preparation). The luminosity and temperature of the X-ray-emitting gas in PNe are satisfactorily reproduced by one-dimensional radiative-hydrodynamic models of the formation of PNe which include thermal conduction at the interface between the shocked wind and the cold outer shell (Steffen et al. 2008). Both observations and models indicate that the X-ray luminosity of PNe decays in short time-scales as the CSPN fades and the nebula expands. For a large, evolved PN such as A 30, no diffuse X-ray emission from the hot bubble enclosed by the AGB wind is expected (Guerrero et al. 2000). Furthermore, we expect the hot bubble to collapse toward the star as it is not supported any longer by the post-AGB wind once it ceased after the VLTP episode.

The correspondence between the spatial distribution of the X-ray emission in A 30 and the cloverleaf structure suggests that the same physical mechanism that generates the X-ray-emitting gas is blowing these petal-like features. The post-born-again stellar wind, with a terminal velocity of $\sim 400 \text{ km s}^{-1}$ for A 30 and a mass-loss rate that could have reached up to $10^{-5} - 10^{-6} M_\odot \text{ yr}^{-1}$, may provide the power to generate the observed X-ray emission. We note, however, that hot bubbles of shocked stellar winds do not form at these wind speeds because of the very efficient line cooling of hydrogen-poor, carbon and oxygen-enriched material (Mellema & Lundqvist 2002; Sandin et al. 2011).

The large momentum and mechanical luminosity of the current fast stellar wind of A 30 can result in strong interactions with the ejecta in hydrogen-poor knots and have the potential to power the observed diffuse X-ray emission. The volume of this cavity, $2.2 \times 10^{54} \text{ cm}^3$, and

the emission measure of the extended component, $2.9 \times 10^{49} \text{ cm}^{-3}$ (Table 3), imply a gas density $N_e = 0.006 \times (\epsilon/0.1)^{-1/2} \text{ cm}^{-3}$, where the gas filling factor ϵ is presumably low. The total mass of the X-ray-emitting gas would be $2 \times 10^{-5} \times (\epsilon/0.1)^{1/2} M_\odot$ and, for a time scale of 850 yr, the averaged mass injection rate of X-ray-emitting gas is $3 \times 10^{-8} (\epsilon/0.1)^{1/2} M_\odot \text{ yr}^{-1}$, which is consistent with the mass-loss rate of the present stellar wind, $2 \times 10^{-8} M_\odot \text{ yr}^{-1}$, derived in Sect. 2.

The temperature of the X-ray-emitting plasma detected in A30, $kT \sim 0.07 \text{ keV}$, is much too low compared to the post-shock temperature expected from a stellar wind with a terminal velocity of 4000 km s^{-1} . Even when heat conduction is considered in models of hot bubbles in PNe, the expected temperature of the X-ray-emitting gas for a wind with such a terminal velocity is in the range $0.13 - 0.43 \text{ keV}$ (Steffen et al. 2008). We note here that the hydrogen-poor, carbon- and oxygen-rich nature of the X-ray-emitting gas implies very efficient line cooling (Mellema & Lundqvist 2002) which can be invoked in conjunction with heat conduction to reduce the temperature of the shocked stellar wind (Steffen et al. 2012).

Alternatively, the origin of such low temperatures lies in the complex interactions between the post-born-again and present fast stellar winds of A 30 and the hydrogen-poor ejecta, as illustrated by the hydrodynamic simulations presented by Steffen & López (2004) and Pittard (2007). The hydrogen-poor knots are photoevaporated by the strong UV radiation flux of the CSPN and subsequently swept-up by the fast stellar winds, which also entrain the H-poor gas ejected after the VLTP episode to form the petal-like features seen in the outer shell. As a result, material with high metal content can be transferred to the shocked stellar wind in three different ways (see Arthur 2007; Pittard 2007): (1) hydrodynamic ablation, (2) conductively-driven thermal evaporation, and (3) photoevaporation. By increasing the density and damping the velocity of the stellar wind, these processes will lower the temperature of the shock-heated stellar wind (e.g., Arthur 2012), which will be further reduced by the efficient cooling of the high metal abundances of the plasma.

5.3. Origin of the X-ray Emission at the CSPN of A 30

If we concur that the point-source of X-ray emission at the CSPN of A 30 originates from a hot plasma, its emission measure, as derived from the spectral fits in Sect. 4.3.3, is $4.8 \times 10^{49} \text{ cm}^{-3}$. Since the emitting region is unresolved by *Chandra*, the emission volume must be smaller than a sphere with radius $0''.5$, i.e., $\sim 1 \times 10^{49} \text{ cm}^3$. These figures imply a density of $4 \epsilon^{-1/2} \text{ cm}^{-3}$ and a total mass of $6 \times 10^{-8} \epsilon^{1/2} M_{\odot}$.

The exact mechanism responsible for the production of X-ray-emitting hot plasma at the CSPN of A 30 is uncertain. Several possibilities are considered in the following.

5.3.1. Photospheric Emission of the Hot CSPN

The photospheric emission from hot ($T_{\text{eff}} > 100,000 \text{ K}$) CSPNe can be detectable in the soft X-ray domain (Guerrero et al. 2000). Since the CSPN of A 30 has an effective temperature of 115,000 K, its X-ray emission may be attributed to photospheric emission. Figure 3 shows the observed SED together with the stellar model presented in Sect. 2. Whereas there is a good match between the observed SED and predicted stellar model in the UV, optical and IR regimes, besides the 2470 Å UV bump, the X-ray flux predicted by the model is ten orders of magnitude lower than the X-ray flux observed by *XMM-Newton*. According to the model, the photospheric X-ray emission is mainly blocked by the bound-free and K-shell opacities from C, N and O. Hence Fig. 3 leads us to the firm conclusion that the stellar photosphere of the CSPN of A 30 cannot be the origin of the observed X-rays.

5.3.2. Shocks Within the Stellar Wind

The stellar winds of CSPNe are radiatively driven, i.e., the stellar wind’s momentum is provided by radiation pressure on spectral lines. We can thus expect that the hydrodynamic instability, which is inherent to radiatively driven stellar winds, will lead to shocks embedded in the stellar wind and produce X-ray emission as for the stellar winds of OB and Wolf-Rayet stars (e.g., Feldmeier et al. 1997). The X-ray luminosity of the stellar wind of O stars is found to scale with the bolometric luminosity as $L_X \approx 10^{-7} L_{\text{bol}}$

(Berghöfer et al. 1997), with a scatter of about one order of magnitude. For this canonical relationship, the stellar luminosity of the CSPN of A 30, $\log L_{\text{bol}}/L_{\odot} = 3.78$ (Table 1) would imply an X-ray luminosity from the wind-shock emission of $10^{-3.2} L_{\odot}$ or $3.5 \times 10^{30} \text{ erg s}^{-1}$. The expected X-ray emission from wind shocks in the CSPN of A 30 is ~ 50 times lower than observed.

Moreover, the aforementioned L_X - L_{bol} relationship is valid for (massive) O stars, but Wolf-Rayet stars are much fainter in the X-ray domain than O stars. Indeed, the first positive detection of faint X-rays from an WC/WO type star has been only recently reported (Oskinova et al. 2009). The most plausible explanation for the X-ray faintness of Wolf-Rayet stars is that their dense winds are very opaque to X-rays, which are presumed to be produced by shocks located in the zone of strong wind acceleration, deep in the wind at a few stellar radii only. To assess whether the wind-shock X-rays could emerge from the [WC]-type central star A 30, we plot in Figure 11 the prediction of our PoWR model of the CSPN of A 30 for the radius where the optical depth reaches unity vs. wavelength. The wind is basically transparent down to the photosphere at 20 Å (0.62 keV), but at longer wavelengths, the opacity increases and the wind stays optically thick out to 7 stellar radii above 50 Å (0.25 keV). The softest X-rays are expected to suffer the strongest attenuation, contrary to the properties of the observed X-ray spectrum. We thus conclude that the X-ray emission from the unresolved central source of A 30 is not due to shocks embedded in its stellar wind.

5.3.3. Born-again Hot Bubble

The mechanical luminosity ($\frac{1}{2} \dot{M} v_{\infty}^2$) of the present stellar wind of the CSPN of A 30 derived from our PoWR model (cf. Table 1), $\approx 1.0 \times 10^{35} \text{ erg s}^{-1}$, is ~ 3000 times larger than the observed X-ray luminosity. A small fraction of this mechanical luminosity would be able to power the X-ray emission which is observed at the central source of A 30. As for the diffuse X-ray emission detected in other PNe, the present stellar wind can be heated when it rams into previously ejected slower material to form a hot bubble. The situation in A 30 is different from other PNe due to its born-again history: while the hot bubble of the old, large PN has faded out, a “born-again hot bubble”, pow-

ered by the present wind, may be responsible of the X-ray emission at the central source. The observed X-ray temperature is however much lower than the expectations for a shocked stellar wind with terminal velocity of 4000 km s^{-1} . Heat conduction and/or mass loading most certainly need to be invoked to cool the plasma to the observed low temperature.

Whereas the origin of the X-ray emission of the CSPN of A 30 in a born-again hot bubble is able to explain its luminosity, there are critical arguments against this scenario. First, the existence of a hot bubble will trap the present fast stellar wind and prevent its interaction with the hydrogen-poor knots; however, this problem can be mitigated by the post-born-again wind which may have contributed mass to the hot plasma. The second argument against the hot bubble scenario is critical. Hot bubbles in PNe fill the whole volume of the innermost shells detected in the optical (Ruiz et al., in preparation), but the X-ray emission arising from the location of the CSPN of A 30 is unresolved by *Chandra*. For a radius of $1.3 \times 10^{16} \text{ cm}$ (i.e., $0''.5$ at the distance of A 30), a hot bubble expanding with the velocity of the post-born-again wind (400 km s^{-1}) requires a time of just 10.5 yr, implying that the transition from the post-born-again wind to the present fast stellar wind occurred some time in 1999. This is at odds with the similar X-ray fluxes detected by *ROSAT* PSPC on 1993 May and *XMM-Newton* EPIC on 2009 October, and is definitely not supported by the quick transition between the post-born-again and fast stellar winds observed in A 58 (Clayton et al. 2006). We conclude that an unresolved born-again hot bubble is difficult to sustain as the origin of the X-ray emission at the CSPN of A 30.

5.4. Charge Transfer Processes

The spectral analysis described in Sect. 4.3.4 and summarized in Table 4 implies that the observed *XMM-Newton* EPIC spectra of A 30 can be reproduced by a model consisting only of C v, C vi and O vii lines. Such spectral characteristics are expected if the X-ray emission is produced by charge transfer from the ions of the stellar wind to material of the hydrogen-poor knots or onto the surfaces of dust grains, as in solar system comets (Krasnopolsky 1997; Lisse et al. 1999;

Dennerl 2010).

As for charge transfer reactions between the stellar wind and neutral material of the hydrogen-poor knots, these are unlikely as we expect the knots to be surrounded by dense ionized outflows (Harrington & Feibelman 1984; Borkowski et al. 1995) that will impede the stellar wind to penetrate deep into the neutral core of the knot. Ion-ion charge transfer processes, considered for the production of X-ray emission in the winds of hot stars (Pollock 2012), is plausible as the large kinetic energy of the ions in the stellar wind of A 30 can overcome the Coulomb repulsion of carbon and oxygen ions in the knots. On the other hand, neutralization of highly ionized ions on the surface of dust grains (e.g., Borkowski & Szymkowiak 1997) can operate because the production of hot dusty plasmas can be expected in the interaction of the fast wind with the born-again ejecta.

We note that these processes must compete with others that can be presumably important, such as recombinations of the ions of the stellar wind that will reduce the number of available highly-ionized species. An upper limit of the X-ray luminosity produced by charge transfer reactions can be computed from the following relation (Dennerl 2010):

$$L_X \sim v_\infty n_w y_X E_X S_k \quad (1)$$

where v_∞ is the wind terminal velocity, n_w is the wind ion density at the location of the neutral material, y_X is the fraction of ions capable of releasing an X-ray photon in a charge-exchange reaction, E_X is the photon energy, and S_k is the cross-section of the hydrogen-poor knots. The terminal velocity of the wind ranges from 400 km s^{-1} for the post-born-again wind up to 4000 km s^{-1} for the present fast stellar wind, whereas their ion density ranges from 10 to 0.001 cm^{-3} , respectively. According to the spectral fit carried out in Sect. 4.3.4, the spectrum of the diffuse emission of A 30 is dominated by the C v 0.31 keV line. Using the energy of the C v line, assuming all carbon atoms are found as C vi with a particle fraction of 0.09 derived from the chemical abundances of the wind, and adopting a ring-like structure $5''$ in radius and $0''.5$ tall for the estimate of the cross-section, the expected X-ray luminosity is $2.6 \times 10^{29} \text{ erg s}^{-1}$ for the present fast stellar wind and $2.6 \times 10^{32} \text{ erg s}^{-1}$ for the post-born-again wind. These figures show

that the post-born-again wind may produce significant X-ray emission through charge transfer reactions, whereas the present fast stellar wind can not.

A similar result can be reached for the X-ray emission at the CSPN, where the greater density of the stellar wind at close locations of the CSPN (0.12 cm^{-3} at $0''.5$ from the CSPN) is compensated by the smaller cross-section, so that the maximum attainable X-ray luminosity would be $\sim 5.7 \times 10^{30} \text{ erg s}^{-1}$. We conclude that, albeit charge transfer can play a role in the production of some the observed X-ray emission, it is unlikely that this mechanism is solely responsible for all observed X-ray flux at the CSPN.

6. Conclusions

We have used *Chandra* and *XMM-Newton* X-ray observations and *HST* multi-epoch archival images of A 30 to investigate the hot gas content and the expansion of the innermost regions of this born-again PN. Optical and UV high-dispersion spectra have been used, in conjunction with the PoWR non-LTE model atmosphere code, to derive the stellar and wind properties of its central star.

The large, nearly spherical outer shell of low density of A 30 meets the expectations of the ISW model of PN formation for an old, evolved object, in agreement with its kinematical age of 10,000–13,000 yr. Since then, the CSPN of A 30 experienced a VLTP event and ejected highly processed material that is detected as large amounts of carbon-rich dust and a series of hydrogen-poor, carbon- and oxygen-rich knots distributed along an expanding equatorial disk and two bipolar outflows. The determination of the proper motions of these knots has allowed us to derive their expansion rate and to obtain an expansion age of $850_{-150}^{+280} \text{ yr}$ that we interpret as the lapse of time since the born-again event.

The CSPN of A 30 presently exhibits a fast stellar wind with terminal velocity $\sim 4000 \text{ km s}^{-1}$ and a low mass-loss rate, $\sim 2 \times 10^{-8} M_{\odot} \text{ yr}^{-1}$. A careful examination of archival [O III] echelle data of A 30 reveals the occurrence of faint nebular features along the line of sight of the CSPN and the cloverleaf-shaped filaments that expand at speeds up to 400 km s^{-1} . These features can be inter-

preted as the signatures of the post-born-again wind. A comparison with the other known born-again CSPNe (A 58, A 78 and VV4334 Sgr) suggests that the onset of the post-born-again wind occurred soon after the born-again event, with time-scales as short as a few years. This post-born-again wind is soon superseded by the present fast stellar wind. Whereas this is an incomplete picture of the evolution of the stellar wind during the born-again and post-born-again phases, we note that the present model calculations do not offer a more detailed view of this transition.

The above descriptions indicate that A 30 is a complex object composed of a system of three nested winds: a post-AGB wind that formed a typical PN shell, a medium-speed born-again and post-born-again wind consisting of processed, hydrogen-poor material, and a present high-speed, hydrogen-poor wind. A 30 is thus a unique system to study the effects of various types of wind-interactions.

The exquisite spatial resolution of *Chandra* and unprecedented sensitivity of *XMM-Newton* have allowed us to resolve the X-ray emission from A 30 into a point-source at its central star and diffuse emission associated with the innermost hydrogen-poor knots and with the cloverleaf structure inside the nebular shell. The diffuse X-ray emission from A 30 originates in the interactions of the present fast stellar wind and post-born-again wind with the hydrogen-poor ejecta. After the born-again event, the hydrogen-poor, carbon-rich post-born-again wind blew a cavity into the nebula that resulted in the cloverleaf structure. The interactions of this wind and the present fast stellar wind with clumps of low speed and carbon-rich dust from the born-again event result in processes of shock-heating and mass-loading of the stellar winds and ablation of the hydrogen-poor knots that produce X-ray-emitting plasma. Diffuse X-ray emission may also result from charge transfer reactions between the stellar winds and the hydrogen-poor ejecta in knots and dust.

The origin of the point-source of X-ray emission at the central star of A 30 is unclear. It is unlikely to result from shocks in the stellar wind, as in OB stars, or from the hot CSPN photospheric emission. The development of a “born-again hot bubble” may explain this emission, but its small size is puzzling.

M.A.G., N.R., and J.T. are partially funded by grants AYA 2008-01934 and AYA2011-29754-C03-02 of the Spanish MICINN (Ministerio de Ciencia e Innovación) and MEC (Ministerio de Economía y Competitividad). Y.-H.C. and R.A.G. acknowledge the support of NASA grants NNX09AU32G and SAO GO01-12029X. Funding for this research has been provided by DLR grant 50OR1101 (LMO). We are grateful to an anonymous referee for pointing out the importance of charge transfer on dust and for detailed comments on charge transfer which significantly improved the manuscript. We are very grateful to Ralf Napiwotzki for providing us with the optical high-dispersion spectra of the central star of A 30 and to Sarah J. Arthur for helpful discussion on charge transfer to dust and ions.

Facilities: Chandra (ACIS-S), HST (WFPC2), KPNO, Spitzer (IRAC). VLT UT2 (UVES), XMM-Newton (EPIC-pn, EPIC-MOS, RGS).

REFERENCES

- Althaus, L. G., Serenelli, A. M., Panei, J. A., et al. 2005, *A&A*, 435, 631
- Arnaud, K.A. 1996, *Astronomical Data Analysis Software and Systems V*, 101, 17
- Arthur, S. J. 2007, *Diffuse Matter from Star Forming Regions to Active Galaxies*, 183
- Arthur, S. J. 2012, *MNRAS*, in press
- Balick, B. 1987, *AJ*, 94, 671
- Beiersdorfer, P., Boyce, K. R., Brown, G. V., et al. 2003, *Science*, 300, 1558
- Berghöfer, T. W., Schmitt, J. H. M. M., Danner, R., & Cassinelli, J. P. 1997, *A&A*, 322, 167
- Bodewits, D., Juhász, Z., Hoekstra, R., & Tielens, A. G. G. M. 2004, *ApJ*, 606, L81
- Borkowski, K. J., Harrington, J. P., Blair, W. P., & Bregman, J. D. 1994, *ApJ*, 435, 722
- Borkowski, K. J., Harrington, J. P., & Tsvetanov, Z. I. 1995, *ApJ*, 449, L143
- Borkowski, K. J., & Szymkowiak, A. E. 1997, *ApJ*, 477, L49
- Cahn, J. H., Kaler, J. B., & Stanghellini, L. 1992, *A&AS*, 94, 399
- Cardelli, J.A., Clayton, G.C., & Mathis, J.S. 1989, *ApJ*, 345, 245
- Cerruti-Sola, M., & Perinotto, M. 1985, *ApJ*, 291, 237
- Chu, Y.-H., Chang, T.H., & Conway, G.M. 1997, *ApJ*, 482, 891
- Chu, Y.-H., Guerrero, M. A., Gruendl, R. A., Williams, R. M., & Kaler, J. B. 2001, *ApJ*, 553, L69
- Chu, Y.-H., & Ho, C.-H. 1995, *ApJ*, 448, L127
- Ciardullo, R., Bond, H. E., Sipior, M. S., et al. 1999, *AJ*, 118, 488
- Cohen, M., Hudson, H. S., Odell, S. L., & Stein, W. A. 1977, *MNRAS*, 181, 233
- Clayton, G. C., Kerber, F., Pirzkal, N., et al. 2006, *ApJ*, 646, L69
- Dennerl, K. 2010, *Space Sci. Rev.*, 157, 57
- Dennerl, K., Englhauser, J., & Trümper, J. 1997, *Science*, 277, 1625
- Duerbeck, H. W., & Benetti, S. 1996, *ApJ*, 468, L111
- Ercolano, B., Barlow, M. J., Storey, P. J., et al. 2003, *MNRAS*, 344, 1145
- Eyres, S. P. S., Smalley, B., Geballe, T. R., et al. 1999, *MNRAS*, 307, L11
- Feldmeier, A., Puls, J., & Pauldrach, A. W. A. 1997, *A&A*, 322, 878
- Greenstein, J. L. 1981, *ApJ*, 245, 124
- Groenewegen, M. A. T., & Lamers, H. J. G. L. M. 1989, *A&AS*, 79, 359
- Guerrero, M. A., Chu, Y.-H., & Gruendl, R. A. 2000, *ApJS*, 129, 295
- Guerrero, M. A., & Manchado, A. 1996, *ApJ*, 472, 711
- Hamann, W.-R., & Gräfener, G. 2004, *A&A*, 427, 697

- Hamann, W.-R., & Koesterke, L. 1998, *A&A*, 335, 1003
- Harrington, J. P., & Feibelman, W. A. 1984, *ApJ*, 277, 716
- Hart, A., Hora, J., Cerrigone, L., et al. 2011, Asymmetric Planetary Nebulae 5 conference, eds. A.A. Zijlstra, F. Lykou, I. McDonald, and E. Lagadec, Jodrell Bank Centre for Astrophysics, 18
- Herwig, F., Blöcker, T., Langer, N., & Driebe, T. 1999, *A&A*, 349, L5
- Iben, I., Jr., Kaler, J. B., Truran, J. W., & Renzini, A. 1983, *ApJ*, 264, 605
- Iben, I., Jr., & MacDonald, J. 1995, *White Dwarfs*, 443, 48
- Jacoby, G.H. 1979, *PASP*, 91, 754
- Jacoby, G. H., & Ford, H. C. 1983, *ApJ*, 266, 298
- Jeffery, C. S. 1995, *A&A*, 299, 135
- Kastner, J. H., Soker, N., Vrtillek, S. D., & Dgani, R. 2000, *ApJ*, 545, L57
- Krasnopolsky, V. 1997, *Icarus*, 128, 368
- Kwok, S., Purton, C. R., & Fitzgerald, P. M. 1978, *ApJ*, 219, L125
- Lawlor, T. M., & MacDonald, J. 2006, *MNRAS*, 371, 263
- Leuenhagen, U., Koesterke, L., & Hamann, W.-R. 1993, *Acta Astronomica*, 43, 329
- Lisse, C. M., Christian, D., Dennerl, K., et al. 1999, *Icarus*, 141, 316
- Lisse, C. M., Dennerl, K., Englhauser, J., et al. 1996, *Science*, 274, 205
- López, J.A., Richer, M.G., García-Díaz, M.T., et al. 2012, *Revista Mexicana Astronomía y Astrofísica*, vol 48, 3
- Meaburn, J., & López, J.A. 1996, *ApJ*, 472, L45
- Meaburn, J., López, J.A., Bryce, M., & Redman, M.P. 1998, *A&A*, 334, 670
- Mellema, G., & Lundqvist, P. 2002, *A&A*, 394, 901
- Miller Bertolami, M. M., & Althaus, L. G. 2006, *A&A*, 454, 845
- Miller Bertolami, M. M., Althaus, L. G., Serenelli, A. M., & Panei, J. A. 2006, *A&A*, 449, 313
- Orio, M., Hartmann, W., Still, M., & Greiner, J. 2003, *ApJ*, 594, 435
- Oskinova, L. M., Hamann, W.-R., Feldmeier, A., Ignace, R., & Chu, Y.-H. 2009, *ApJ*, 693, L44
- Perinotto, M., Schönberner, D., Steffen, M., & Calonaci, C. 2004, *A&A*, 414, 993
- Phillips, J. P., & Ramos-Larios, G. 2007, *AJ*, 133, 347
- Pittard, J. M. 2007, *Diffuse Matter from Star Forming Regions to Active Galaxies*, 245
- Pollock, A.M.T. 2012, *AN*, 333, 351
- Reed, D. S., Balick, B., Hajian, A. R., et al. 1999, *AJ*, 118, 2430
- Sandin, C., Steffen, M., Schönberner, D., Rühling, U., & Hamann, W. R. 2011, Asymmetric Planetary Nebulae 5 conference, held in Bowness-on-Windermere, U.K., 20 - 25 June 2010, A. A. Zijlstra, F. Lykou, I. McDonald, and E. Lagadec, eds. (2011) Jodrell Bank Centre for Astrophysics,
- Schönberner, D., Jacob, R., Sandin, C., & Steffen, M. 2010, *A&A*, 523, A86
- Schönberner, D., Jacob, R., & Steffen, M. 2005a, *A&A*, 441, 573
- Schönberner, D., Jacob, R., Steffen, M., et al. 2005b, *A&A*, 431, 963
- Seitter, W. C. 1987, *The Messenger*, 50, 14
- Steffen, M., Sandin, C., Jacob, R., & Schönberner, D. 2012, in *IAU Symp. 283, Planetary Nebulae, an Eye to the Future*, ed. A. Manchado, D. Schönberner, & L. Stanghellini (Cambridge: Cambridge Univ. Press), in press
- Steffen, M., Schönberner, D., & Warmuth, A. 2008, *A&A*, 489, 173
- Steffen, W., & López, J. A. 2004, *ApJ*, 612, 319

Todt, H., Hamann, W.-R., & Gräfener, G. 2008,
Clumping in Hot-Star Winds, 251

Tyne, V. H., Evans, A., Geballe, T. R., et al. 2002,
MNRAS, 334, 875

Wesson, R., Liu, X.-W., & Barlow, M. J. 2003,
MNRAS, 340, 253

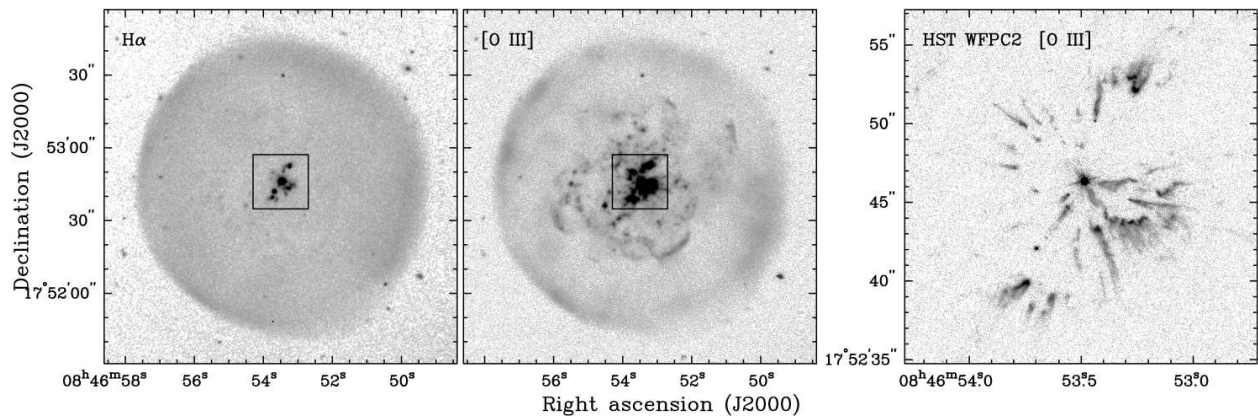


Fig. 1.— KPNO Mayall 4m CCD H α (*left*), [O III] (*center*), and *HST* WFPC2 [O III] (*right*) images of A 30. The boxes overlaid in the ground-based images correspond to the field of view of the *HST* image shown. The ground-based images were acquired through filters with central wavelengths 5025 Å and 6580 Å, and FWHMs 50 Å and 60 Å, respectively; the *HST* WFPC2 image used the F502N filter.

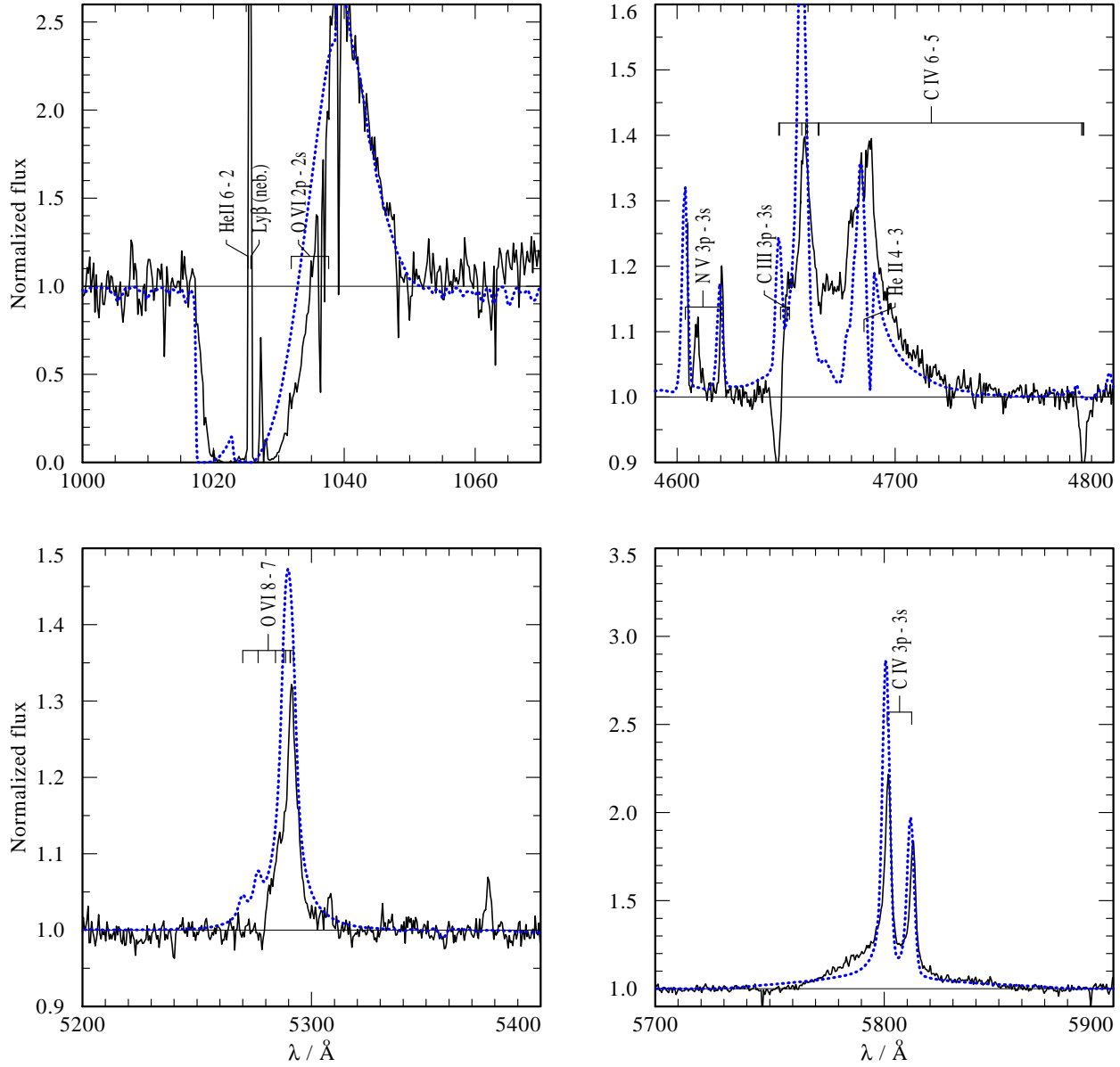


Fig. 2.— Some of the spectral lines employed for the spectral analysis of the central star of A 30. Observations (solid line) are from *FUSE* and from ground-based spectroscopy. The synthetic spectrum (dotted line) has been calculated with the Potsdam Wolf-Rayet (PoWR) model atmosphere code, using the parameters compiled in Table 1.

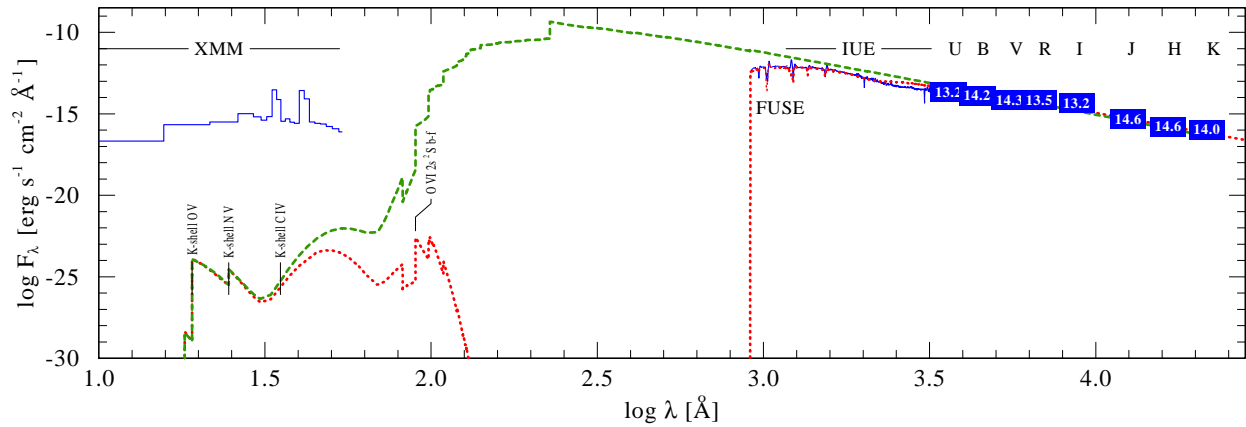


Fig. 3.— Spectral energy distribution (SED) of the central star of A 30 from the infrared to X-ray range. Observations (blue) are photometric measurements in the indicated bands, calibrated UV spectra from the *IUE* and *FUSE* satellites, and the *XMM-Newton* observations reported in this paper. These measurements are compared to the theoretical SED from our stellar model with the parameters compiled in Table 1. The green dashed line shows the SED without interstellar reddening, and the red dotted line after interstellar extinction has been applied.

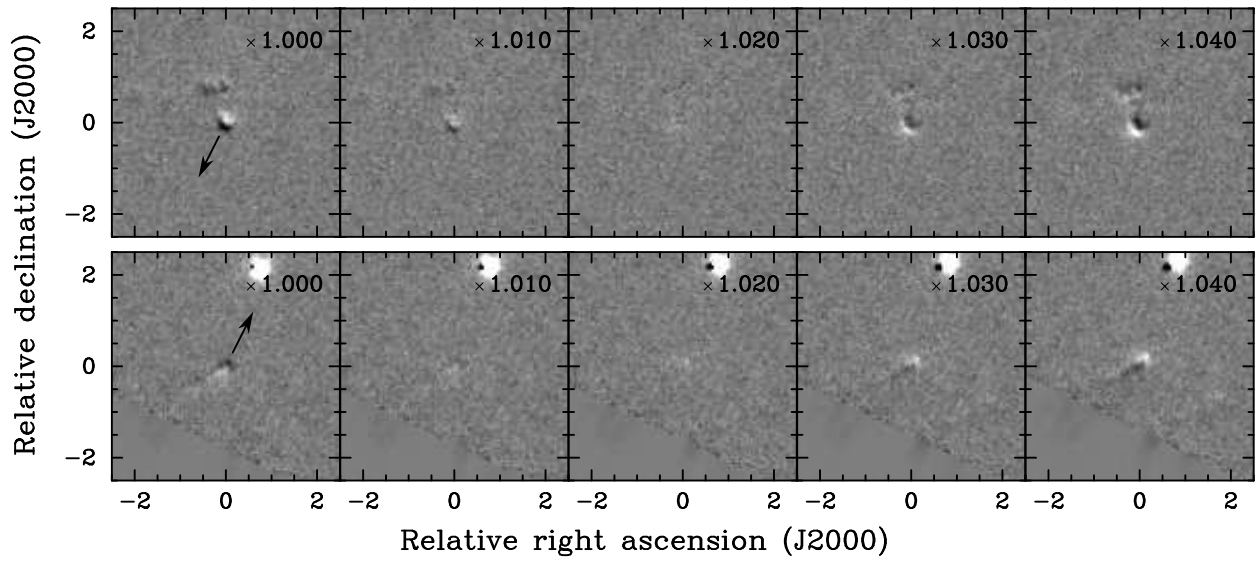


Fig. 4.— Residual maps of the northern (upper panels) and southern (lower panels) hydrogen-poor bipolar knots of A 30, where the F502N image has been magnified by the factor noted in each panel. Dark shades correspond to the F502N March 1994 image and bright shades to the F555W December 2009 image. The direction of the central star is marked by an arrow in the leftmost panels.

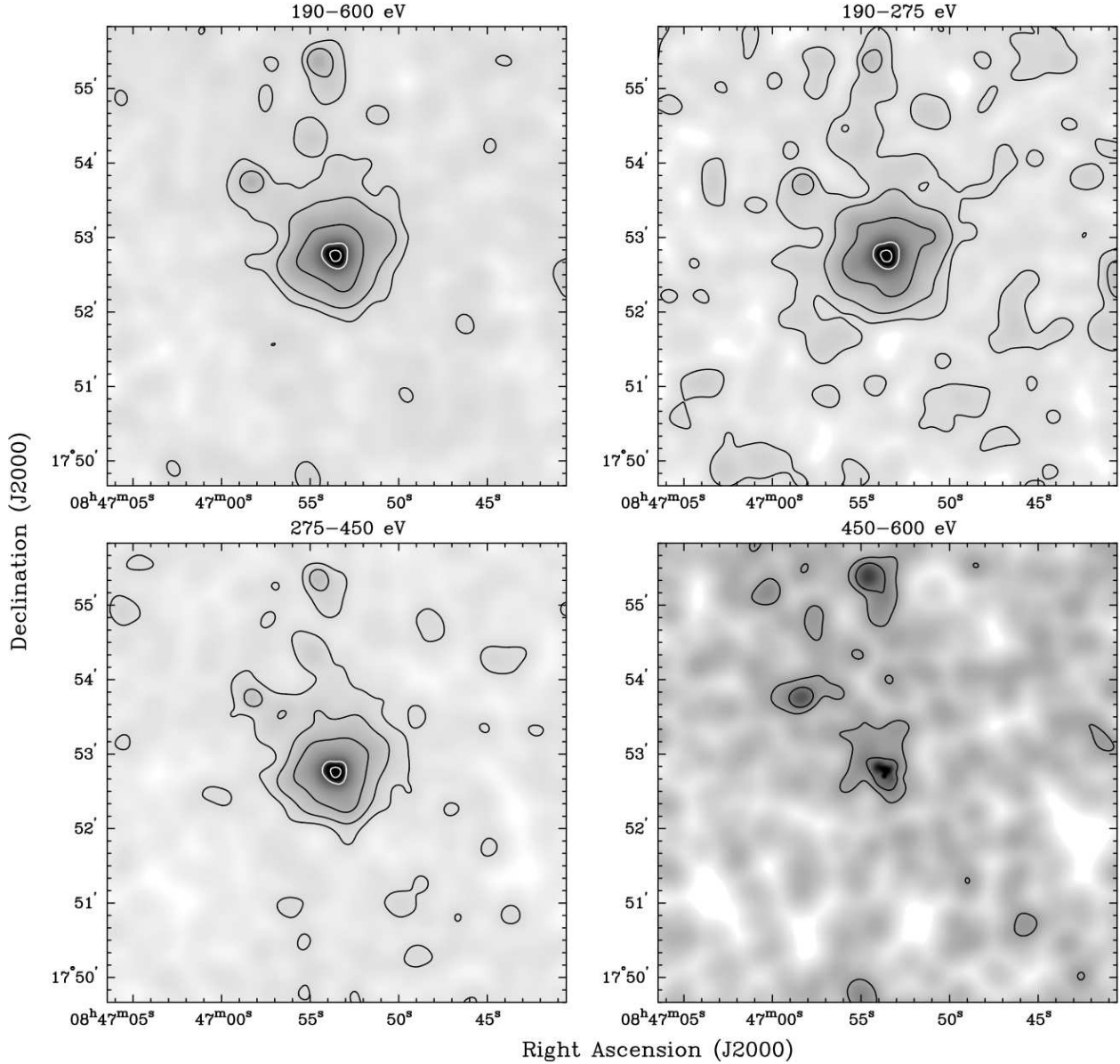


Fig. 5.— Exposure-corrected *XMM-Newton* EPIC images of A30 in different energy bands. The images have a pixel size 1'' and have been smoothed using an adaptive Gaussian kernel with sizes between 1'' and 8''. Gray-scales have been chosen in the range between 15 σ below the background level and 20% of the intensity peak for each image. The black lower contours correspond to 5 σ , 10 σ , and 30 σ over the background level, while the white upper contours represent 10% and 50% of the peak intensity.

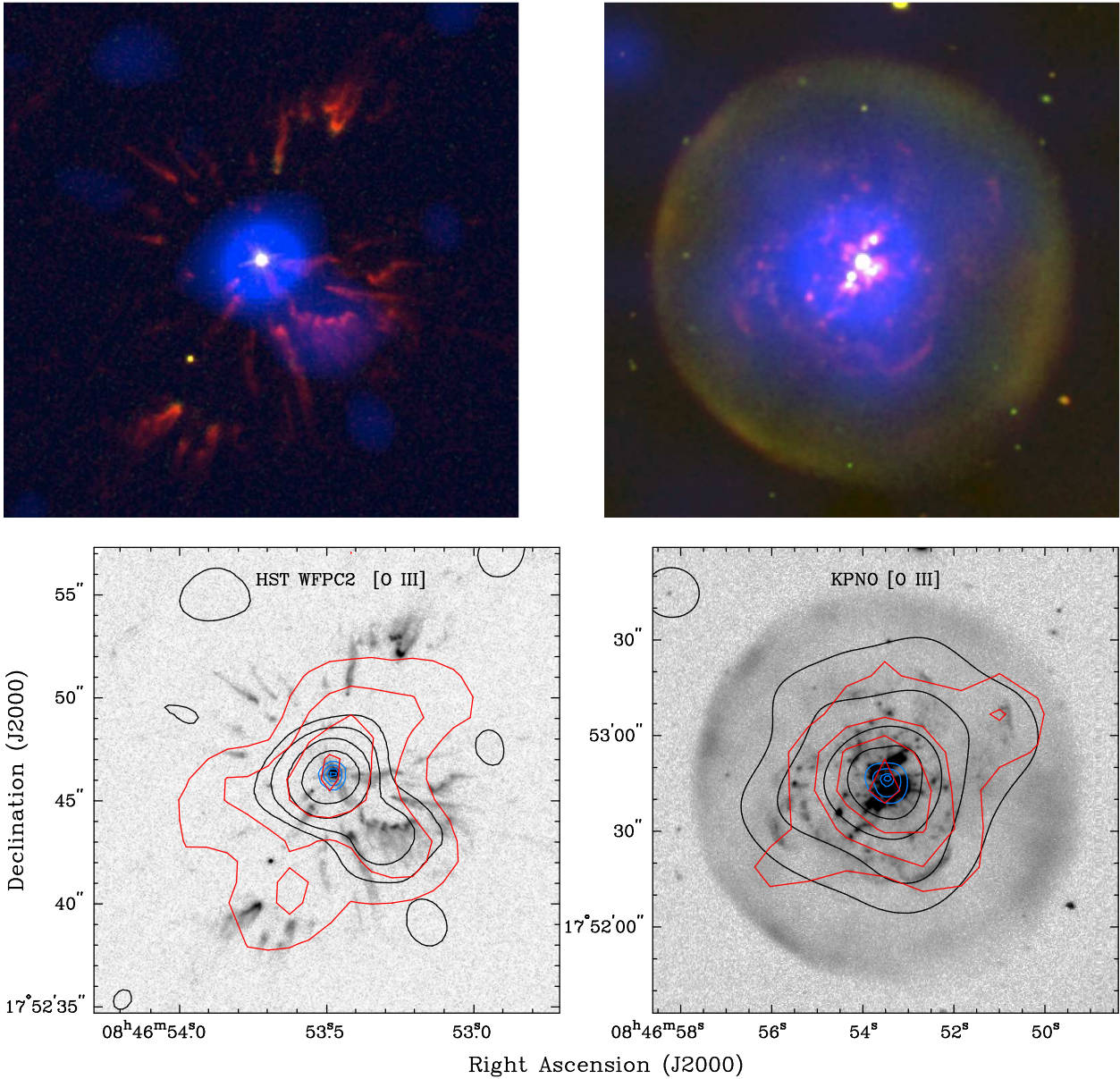


Fig. 6.— Comparison of narrow-band optical and X-ray images of A 30. (*top*) Color-composite images: the *HST* WFPC2 (RED=[O III], GREEN=He II) and *Chandra* ACIS-S 0.20-0.60 keV (BLUE) composite in the left panel illustrates the small-scale spatial distribution of X-rays, whereas their large-scale spatial distribution is shown by the ground-based (RED=[O III], GREEN=H α) and *XMM-Newton* 0.19-0.60 keV (BLUE) composite in the right panel. (*bottom*) Optical [O III] narrow-band images of A 30 overplotted by X-ray contours: *HST* WFPC2 image overplotted by *Chandra* ACIS-S (blue and black) and *ROSAT* HRI (red) contours (*left*) and ground-based image overplotted by *XMM-Newton* EPIC (blue and black) and *ROSAT* PSPC (red) contours (*right*). Red and blue contours have been set at 95%, 75%, 50%, and 25% of the peak intensity, whereas the black contours correspond to 5σ , 10σ , 25σ , and 100σ above the background level for the *Chandra* ACIS-S image, and 10σ , 25σ , 50σ , and 100σ above the background level for the *XMM-Newton* EPIC image.

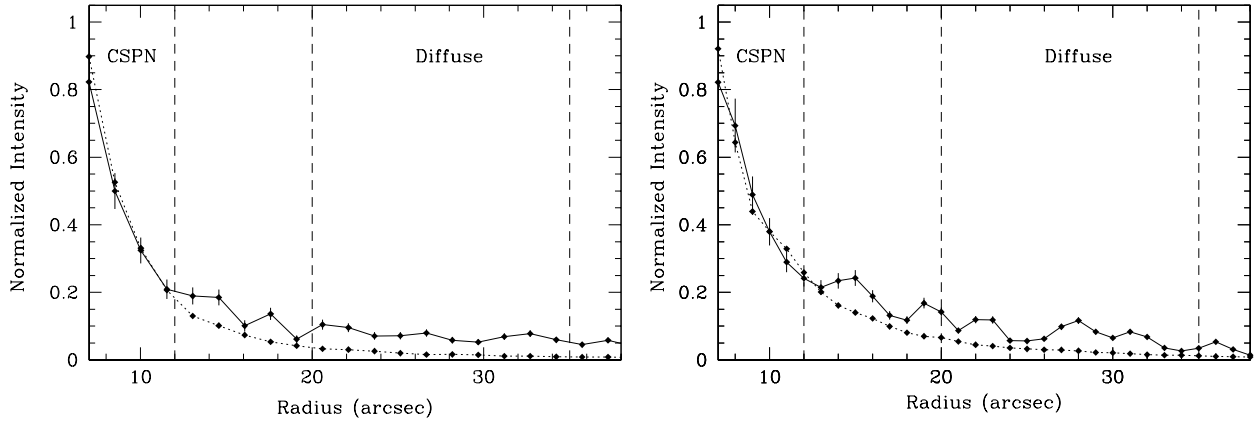


Fig. 7.— Comparison of the EPIC-pn radial profiles of A 30 (solid line) and Nova LMC1995 (dotted line) as extracted using “eradial” (*left*) and by deriving the count rate in annular regions (*right*). The vertical dashed lines mark the source regions for the extraction of the X-ray spectra of the CSPN and diffuse emission.

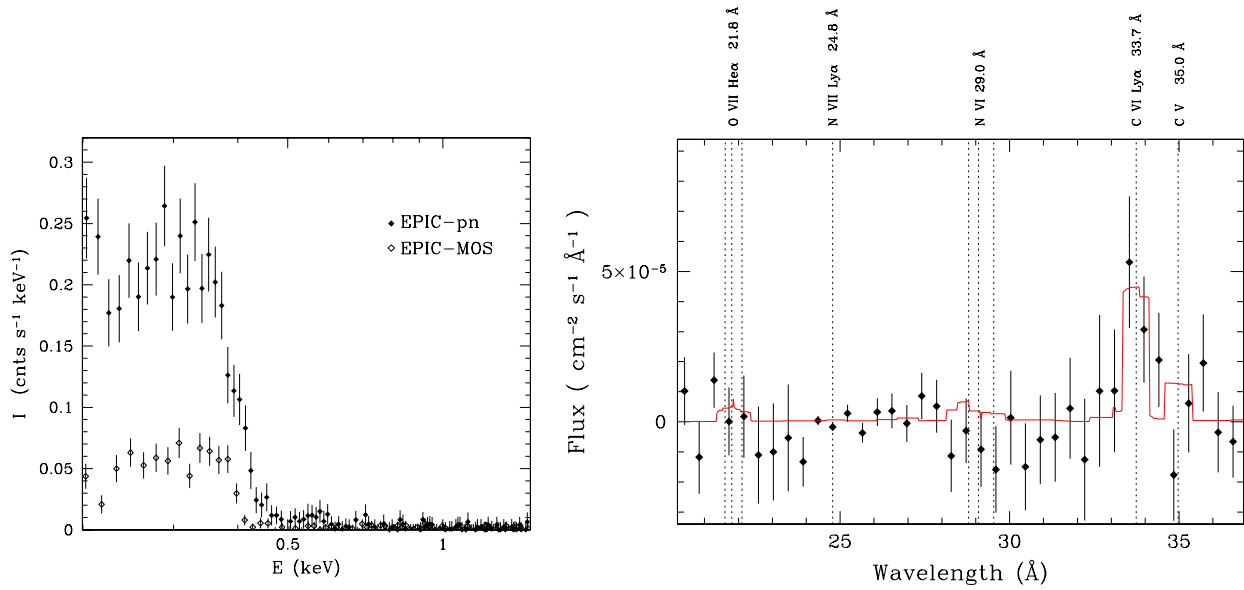


Fig. 8.— *XMM-Newton* EPIC (*left*) and combined RGS1+RGS2 (*right*) background-subtracted spectra of A 30. The EPIC spectra have been extracted from a circular aperture of radius $35''$ centered on A 30, while the RGS spectrum has been extracted using the standard RGS aperture. The red histogram overplotted on the (*right*) panel corresponds to the plasma emission model described in the text at a similar spectral resolution as that of the RGS spectrum.

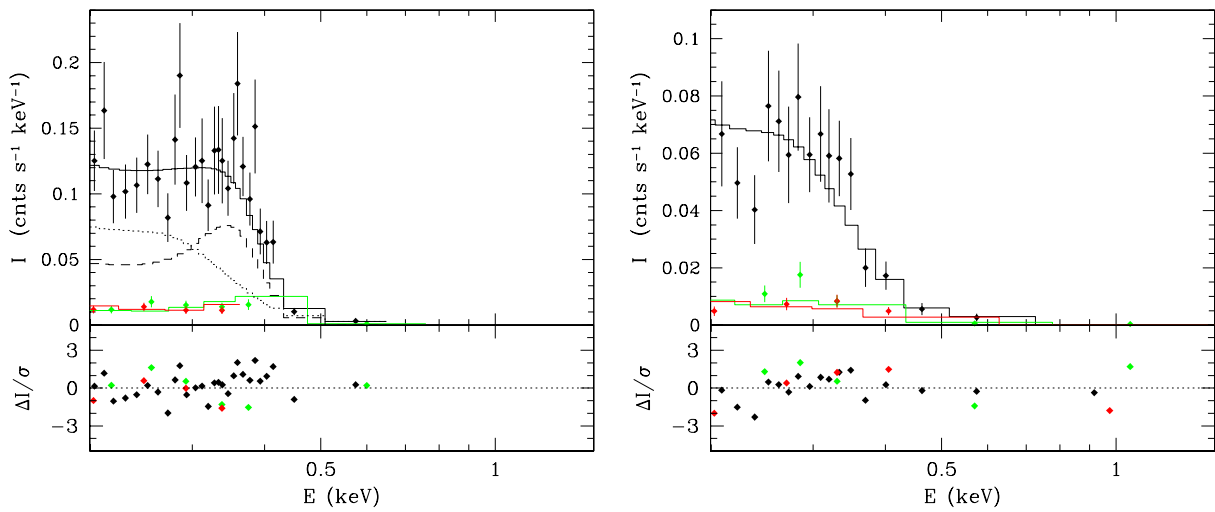


Fig. 9.— EPIC-pn (black), EPIC-MOS1 (green), and EPIC-MOS2 (red) background-subtracted spectra of the central source in A 30 (*left*) and its diffuse emission (*right*). Note the different intensity scale as the spectrum of the diffuse emission is ~ 2.5 times fainter than that of the central source. The solid lines correspond to the best-fit described in the text, with the residuals of the fit shown in the lower panels. For the spectral fit, the channels have been binned to include 20–25 counts per channel. The dotted and dashed lines in the panel of the central star correspond to the thermal emission plasma and emission line components of the EPIC-pn model, respectively.

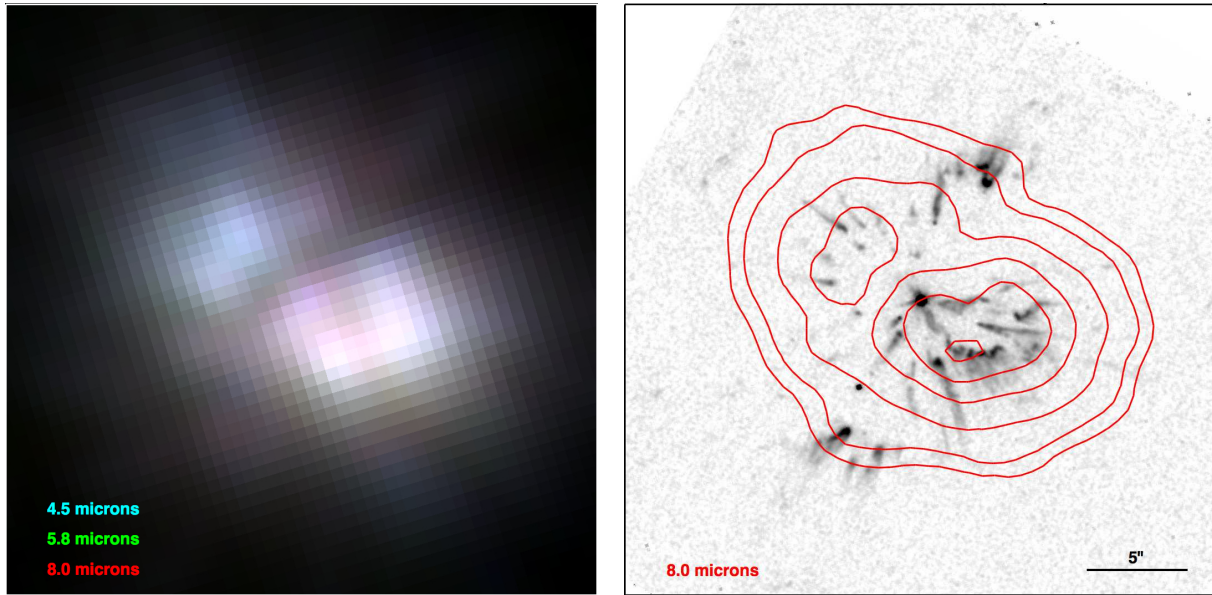


Fig. 10.— Comparison of *HST* [O III] and *Spitzer* IRAC images of the central regions of A 30. (*left*) Color-composite *Spitzer* 4.5 μm (blue), 5.8 μm (green), and 8.0 μm (red) image of A 30 obtained using the IRAC observations 21967616 (PI: G. Fazio). The subtle variations in the color indicates that the spectral energy distribution in the IRAC bands of the dust emission is rather flat, with a subtle 4.5 μm excess in the eastern regions of the equatorial ring and some 8.0 μm excess at the location of the CSPN. (*right*) Grey-scale of the *HST* WFPC2 [O III] image of A 30 overplotted by *Spitzer* IRAC 8.0 μm contours. North is up, east is left. The spatial scale is shown on the *HST* [O III] image.

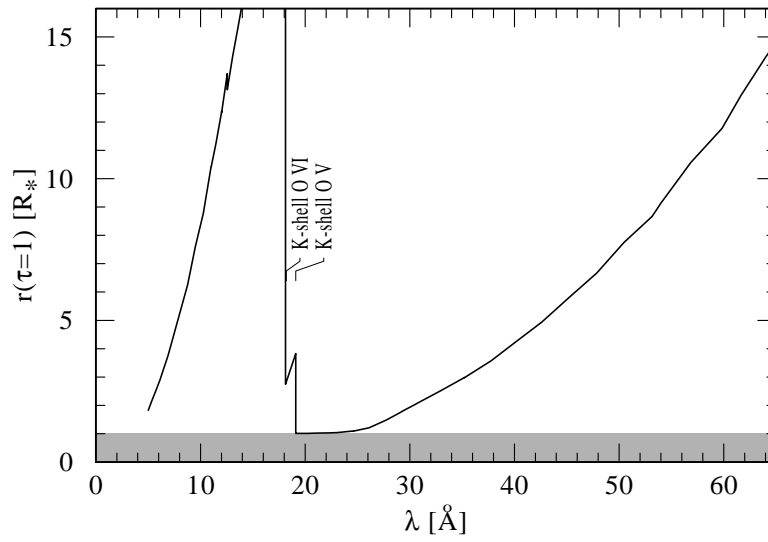


Fig. 11.— Radius where the radial optical depth reaches unity as a function of wavelength according to our PoWR model for the CSPN of A 30 (Table 1). The gray band marks optical depth values below unity. The location of the O V and O VI K-shell have been labeled.

TABLE 1
PARAMETERS OF THE CENTRAL STAR OF A 30

Parameter	Value	Comments
Stellar parameters		
$\log(L/L_{\odot})$	3.78	Adopted
Clumping factor, D	10	Adopted
d (kpc)	1.76	$d \propto L^{1/2}$
E_{B-V} (mag)	0.18	
R_* ^a (R_{\odot})	0.20	$R_* \propto L^{1/2}$
T_* ^b (K)	115,000	
v_{∞} (km s ⁻¹)	4000	
\dot{M} ($M_{\odot} \text{ yr}^{-1}$)	2.0×10^{-8}	$\dot{M} \propto D^{-1/2} L^{3/4}$
Abundances (mass fractions)		
He	0.63	
C	0.20	
N	0.015	
O	0.15	
Fe (+ iron group)	0.0016	

^a The stellar radius R_* refers by definition to the point where the radial Rosseland optical depth is 20.

^b T_* is defined as the effective temperature related to the radius R_* .

TABLE 2
BACKGROUND-SUBTRACTED COUNT RATES AND NET COUNT NUMBERS

Instrument	Background-subtracted count rate				Net counts
	190-600 eV ¹ (counts ks ⁻¹)	190-275 eV (counts ks ⁻¹)	275-450 eV (counts ks ⁻¹)	450-600 eV (counts ks ⁻¹)	190-600 eV ^a (counts)
Point source and diffuse emission					
EPIC-pn	50.4±1.6	19.7±0.9	28.3±1.1	1.57±0.31	1150±40
EPIC-MOS1	7.7±0.6	219±16
EPIC-MOS2	6.6±0.5	186±15
ACIS-S	1.80±0.14	172±13
Point source					
EPIC-pn	29.7±1.1	675±26
EPIC-MOS1	4.4±0.4	140±12
EPIC-MOS2	3.4±0.3	105±10
Diffuse emission					
EPIC-pn	14.3±0.9	325±20
EPIC-MOS1	2.2±0.3	71±9
EPIC-MOS2	1.7±0.3	55±8

^a For ACIS-S, the low energy cutoff is not 190 eV, but 200 eV.

TABLE 3
BEST FIT PARAMETERS FOR PLASMA EMISSION MODELS

Region	N_{H} (cm ⁻²)	kT (keV)	EM ^a (cm ⁻³)	I_{CVI} (photon cm ⁻² s ⁻¹)	$\chi^2/\text{d.o.f.}$
A 30	$(2\pm 2)\times 10^{15}$	0.070±0.005	9.2×10^{49}	...	2.08 (=199.6/96)
CSPN ^b	2×10^{15}	0.068±0.003	4.8×10^{49}	$(5.0\pm 0.6)\times 10^{-5}$	1.11 (=46.5/42)
Diffuse ^b	2×10^{15}	0.068 ^{+0.002} _{-0.005}	2.9×10^{49}	...	1.38 (=42.7/31)

^aEmission measure, $\text{EM} = \int n_e n_{\text{ion}} dV = 10^{14} 4\pi d^2 K_{\text{appec}}$.

^bAdopted value of the hydrogen column density.

TABLE 4
BEST FIT PARAMETERS FOR CHARGE-EXCHANGE REACTION MODELS

Region	N_{H}	I_{CV}	I_{CVI}	I_{NVI}	I_{NVII}	I_{OVII}	I_{OVIII}	$\chi^2/\text{d.o.f.}$
	(cm^{-2})	(photon $\text{cm}^{-2} \text{s}^{-1}$)						
CSPN ^a	2×10^{15}	7.2×10^{-5}	6.7×10^{-5}	$< 1 \times 10^{-8}$	$< 5 \times 10^{-9}$	1.6×10^{-6}	4.7×10^{-8}	1.35 (=37.8/28)
Diffuse ^a	2×10^{15}	4.0×10^{-5}	9.5×10^{-6}	$< 1 \times 10^{-8}$	$< 1 \times 10^{-8}$	7.5×10^{-7}	$< 2 \times 10^{-7}$	1.23 (=49.0/40)

^a Adopted value of the hydrogen column density.